

This is the author's final, peer-reviewed manuscript as accepted for publication (AAM). The version presented here may differ from the published version, or version of record, available through the publisher's website. This version does not track changes, errata, or withdrawals on the publisher's site.

Lightweight, aluminum, mirror design optimization for conventional and additive manufacturing processes

Jitsupa Paenoi, Cyril Bourgenot, Carolyn Atkins, Robert Snell, Iain Todd, Paul White, Kenneth Parkin, David Ryder, Richard Kotlewski, Scott McPhee, Krittapas Chanchaiworawit, Pearachad Chartsiriwattana, Auychai Laoyang, Teerawat Kuha, Apichat Leckngam, Christophe Buisset, Wiphu Rujopakarn, Saran Poshyachinda

Published version information

Citation: J Paenoi et al. 'Lightweight, aluminum, mirror design optimization for conventional and additive manufacturing processes.' Proceedings of SPIE: Advances in Optical and Mechanical Technologies for Telescopes and Instrumentation V, vol. 12188 (2022) 121880U. Is in proceedings of: SPIE Astronomical Telescopes + Instrumentation, Montréal, Québec, Canada, 17-23 Jul 2022.

DOI: [10.1117/12.2627757](https://doi.org/10.1117/12.2627757)

This accepted manuscript is made available under a [CC BY](https://creativecommons.org/licenses/by/4.0/) 4.0 licence. Please cite only the published version using the reference above. This is the citation assigned by the publisher at the time of issuing the AAM. Please check the publisher's website for any updates.

This item was retrieved from **ePubs**, the Open Access archive of the Science and Technology Facilities Council, UK. Please contact epublications@stfc.ac.uk or go to <http://epubs.stfc.ac.uk/> for further information and policies.

Lightweight, aluminum, mirror design optimization for conventional and additive manufacturing processes

Jitsupa Paenoi^{*a}, Cyril Bourgenot^b, Carolyn Atkins^c, Robert Snell^d, Iain Todd^d, Paul White^b,
Kenneth Parkin^b, David Ryder^b, Richard Kotlewski^c, Scott McPhee^c,
Krittapas Chanchaiworawit^a, Pearachad Chartsiriwattana^a, Auychai Laoyang^a,
Teerawat Kuha^a, Apichat Leckngam^a, Christophe Buisset^a, Wiphu Rujopakarn^a, and
Saran Poshyajinda^a

^aNational Astronomical Research Institute of Thailand, Chiang Mai, Thailand

^bDurham University, NETPark Research Institute, Sedgefield, TS21 3FB, UK

^cUK Astronomy Technology Centre, Blackford Hill, Edinburgh, EH9 3HJ, UK

^dDept of Materials Science and Engineering, University of Sheffield, Sheffield, S1 3JD, UK

ABSTRACT

Lightweight, aluminum, freeform prototype mirrors have been designed and fabricated by a Thai led team, with UK support, for intended applications within the Thai Space Consortium (TSC) satellite series. The project motivation was to explore the different design strategies and fabrication steps enabled by both conventional (mill, drill, and lathe) and additive (3D printing) manufacture of the prototype substrates. Single Point Diamond Turning was used to convert the substrates into mirrors and optical metrology was used to evaluate the different mirror surfaces.

The prototype criteria originated from the TSC-1 satellite tertiary mirror, which is designed to minimize the effect of Seidel aberrations before the beam enters the hyperspectral imager. To converge upon the prototype designs, Finite Element Analysis (FEA) was used to evaluate the different physical conditions experienced by the prototypes during manufacture and how these influence the optical performance. The selected designs satisfied the mass and surface displacement criteria of the prototype and were adapted to either the conventional or additive manufacturing process. This paper will present the prototype design process, substrate manufacture, optical fabrication, and an interferometric evaluation of the optical surfaces comparing the conventional and additive manufacturing processes.

Keywords: Finite element analysis, additive manufacture, lightweight mirrors, freeform optics, 3D printing, aluminum

1. INTRODUCTION

1.1 General Introduction

The design of space optical instrumentation faces constraints such as temperature, vacuum, vibration (jitter), weak gravity, and harsh environment. These factors influence choices made at the design level on material, mounting, and manufacturing strategies. One particular benefit offered by metal optics for space systems applications compared to other materials, for instance glass or ceramics, is the prospect of incorporating freeform surfaces into the design while reducing manufacture and assembly costs. Single point diamond turning (SPDT) technology using tool servo can speed up the manufacturing process of freeform with form accuracy of about 20-40 nanometers root mean square (RMS). Another benefit is the potential for ultra-lightweighting and the possibility to incorporate some advanced designs while keeping imaging quality, mass, and volume optimal.

Further author information: (Send correspondence to Jitsupa Paenoi)

J. Paenoi - E-mail: jitsupa@narit.or.th

C. Bourgenot - E-mail: cyril.bourgenot@durham.ac.uk

In this paper, we explore the potential of additive manufacture (AM) to design and fabricate novel types of aluminum mirrors. We are interested in evaluating a range of highly compact designs optimized for both additive and conventional manufacturing techniques. For example, integrating 3 flexible pads into the body of the mirror to isolate the mounting interface from the optical surface. We compared this stress-free “flexible pads” design with the more robust, but heavier, layout called the “Mushroom” design, where the mounting interface is isolated from the optical surface by a gap and connected to the main body by a central bridge.

The main financial support in this project was provided by the Science and Technology Facilities Council (STFC) Newton fund through a Knowledge Transfer Partnership between Durham University, UK Astronomy Technology Centre (UKATC), and the University of Sheffield (UoS) with the National Astronomical Research Institute of Thailand (NARIT). NARIT was the main site for the development, manufacturing, and metrology of mirrors. The project “Towards Freeform Optics Manufacturing Capabilities in Thailand for Space and Astronomical Applications” aimed to train two Thai engineers in conventional and additive manufacturing for space and astronomical applications. NARIT is investigating innovative technologies for the next generation of space astronomy satellites (named TSC satellites) with an objective of developing its own satellite to image the surface of the Moon. TSC-1 is a small scientific satellite under the development of the Thai Space Consortium. NARIT has been commissioned to deliver the primary payload for TSC-1 called the Hyperspectral imager. The instrument will utilize state-of-the-art technologies to achieve Moon surface observation at the expected resolutions and sensitivities.

The case study for this paper is an adaptation of the TSC-1’s tertiary mirror (M3). The original M3 mirror in the TSC-1 optical design is nominally a freeform surface but, in this study, it was approximated to the best fit sphere to facilitate subsequent metrology using phase shifting interferometry with a spherical beam. First, the M3 payload mirror went through a phase of mechanical design to implement a lightweight layout that could be achievable by conventional manufacture (CM) techniques and then, the CM design was adapted for additive manufacture, resulting in three different AM design (Section 2). Finite element analysis (FEA) was used to assess the designs and to ensure that the distortions expected during the manufacture processes would not negatively impact the prototype mirrors (Section 3). Conversion of the selected designs into physical prototypes started with AM (Section 4) and finished with SPDT (Section 5). Finally the AM and CM prototype mirrors were evaluated using interferometry and compared against the FEA prediction (Section 6).

1.2 The Astronomical Applications of Freeform Optics

Freeform optics are novel and revolutionary¹ optical elements with no particular axis of rotation or symmetry. They are increasingly used in pioneering optical designs offering abundant new opportunities for optical designers.² In particular, freeform surfaces help to improve compactness, image sharpness and contrast in a larger field of view. Freeform optics are therefore promising components for airborne or space-based hyperspectral imagers for their ability to reduce the overall dimension, and therefore mass, of the satellite’s payload, which is a critical parameter in space imaging systems.

The freeform reflective surfaces, especially metal, provides various advantages above the conventional mirrors such as their compactness, lightweight, superior image quality, and versatility.³⁻⁷ The first two mentioned aspects of freeform optics directly ease the budget burden of a space mission by requiring less volume and fuel to achieve the scientific goals.^{5,8,9} While the latter aspects suggest that a single freeform surface can perform the same duty as an ensemble of conventional optical components. Thus, the overall throughput of an instrument can be optimized.

As one may be able to deduce, the applications of freeform optics can spread across various fields of astronomy from studying the diffuse light of the local intra-cluster stars to the newborn galaxies in the early Universe. Beating the noise level and the artifacts from the field distortions,⁴ only freeform surfaces can provide us with such an opportunity to efficiently observe the low surface-brightness Universe.

Many state-of-the-art ground-based observatories use freeform optics to some degree.¹⁰⁻¹² For instance, the GNIRS instrument at Gemini Telescope incorporated a monolithic image-slicer constructed from a grooved-freeform surface¹² for its Integrated-Field-Unit (IFU) unit to reduce the complication of the alignment process and increase the overall throughput. Furthermore, compact and light freeform surfaces are essential for the recent

and next-generation space missions. For example, James Webb Space Telescope (JWST) has utilized multiple freeform-surface beryllium mirrors (from primary to tertiary mirrors) to optimize the visible field-of-view (FOV), reduce alignment dependent on the image quality, maintain high throughput while minimizing the total weight of the telescope.¹³ The instruments on board the JWST such as Near Infrared Camera¹⁴ (NIRCam) and Near Infrared Spectrograph¹⁵ (NIRSpec) also adopted freeform surfaces to reduce the number of surfaces and minimize distortions near the edges of the FOV. In addition, freeform optical components are proven vital to the success of a number of other space missions.^{4,5,8} Therefore, a space mission that prioritizes the use of freeform optics would be more fuel efficient and able to satisfy its scientific goals within a shorter amount of time. But, to achieve freeform surfaces with the desired capabilities, one requires cutting-edge manufacturing process that the current technology can offer to build sturdy, yet light and compact optical components.

The emergence of these new types of surfaces has been very much in pace with the development of Single Point Diamond Turning (SPDT) using Tool Servo. SPDT is an attractive methodology for freeform surfaces due to its ability deterministically to produce submicron accuracy, large dimensions and complex surfaces with significant sag.

1.3 Additive Manufacture and Astronomical Mirrors

AM, commonly known as 3D printing, is a manufacturing method that creates an object layer-by-layer from a digital design file. The primary advantage of AM is the design freedom that is available, because the process is additive, rather than subtractive, lattices and organic geometries can be created with relative ease. AM is not limited to extruded plastics, a broad range of engineering polymers, ceramics, metals and composites are available. However, AM is not without challenges, a lack standardisation between different printers and print parameters (the settings used by the printer) can result in two components created in the same material on similar printers having different material properties. Furthermore, implementing AM requires a shift in the conventional design \rightarrow manufacture process flow, which typically results in an increase in time to create components due to a lack of experience in this manufacturing method in comparison to conventional manufacture.

AM is ideal manufacturing method for low part counts, mass reduction and part consolidation (combining individual components into a single component), as such, AM is an ideal manufacturing method for astronomical hardware which tends to be bespoke and complex in design and operation.¹⁶ Bespoke metallic lightweight mirrors, frequently used in astronomical hardware, are a clear candidate for redesign using AM. In this case, the benefits of AM in terms of design can result in lightweight mirrors that are optimised for function, rather than designed to allow subtractive manufacturing. Numerous institutes are actively researching metallic AM mirrors and how the benefit of design freedom can be harnessed.¹⁷ Early prototyping explored the ability of the AM substrate to be polished or single point diamond turned,¹⁸⁻²⁰ more recently application specific prototypes have been manufactured that include novel lightweight structures and part consolidation.²¹⁻²⁵ To date, the optical quality of AM mirrors is variable, by directly processing AM aluminium alloys using SPDT, the surface roughness values range from ~ 3 nm to 10 nm RMS,^{21,25-28} further improvements in surface roughness can be achieved by coating the AM aluminium substrate in nickel phosphorus and following the SPDT with a polishing phase.²⁴ Considering form error across the optical aperture, where SPDT alone has been applied directly to the AM aluminium substrate, RMS values from ~ 30 nm to 60 nm are frequently achieved.^{21,25,27} The development of AM mirrors is on-going within the community to utilise the benefits of the AM design freedom whilst understanding the ideal post-processing route to achieve the optimum optical quality, and ultimately, optical performance.

2. AM DESIGN AND CASE STUDY DESCRIPTION

The task of designing the M3 mirror of the TSC-1's payload is a starting point of this project. We designed and manufactured the M3 prototypes using both CM and AM. The AM process chain is illustrated in Figure 1, explaining the entire manufacturing process starting from designing, where the optical surface and the overall construct were defined utilizing ZEMAX to Solidworks, respectively. We then verified the design by testing its alignment and cooperation with the whole optical system of what would be TSC-1's payload. To reduce the total mass of each design, we took two different approaches, thus born two distinct model series, namely Mushroom and Flexible Pads designs. The Mushroom design consists of a lattice structure between the optical surface and the base. While Flexible Pads design has flexible pads added to its base as the name suggested. One of the main

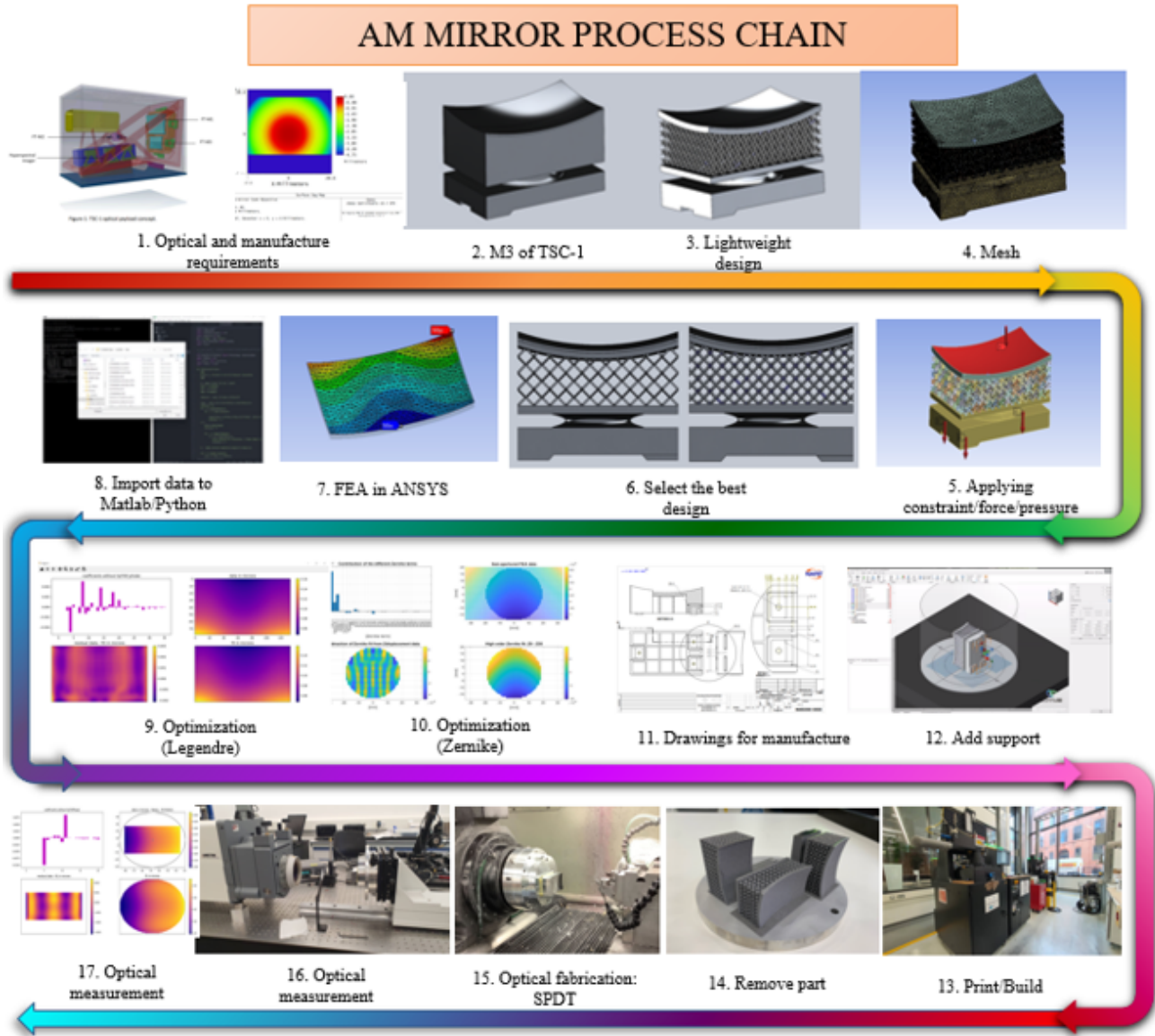


Figure 1. This process chain presents the Additive manufacturing process of the TSC-1 M3 mirror. Started with optical and mechanical requirements until optical measurement and testing.

goals of this study was to limit the impact of the manufacturing process, such as Computer Numerical Control: Single Point Diamond Turning (CNC: SPDT), on the optical surface. We used the FEA function in the ANSYS program to simulate the surface displacement after applying physical constraints (i.e., force and pressure) before creating a mesh. According to the FEA results, we selected the model which provided minimal displacements. Then, we transfer the displacement data of the FEA on the optical surface from ANSYS to Python for performing Legendre and Zernike optimization. Using Aconity software, we prepared the finalized model for 3D printing. We loaded the metal powder needed for printing the prototype. After a successful printing process, we apply the fly cut process to trim and clean the pads and base of the prototype to get it ready for the SPDT. Finally, we verified the sharpness and roughness of the optical surface using an interferometer.

2.1 Origin of Design

In this pilot study, we selected to build the tertiary mirror (M3) of TSC-1’s payload due to its requirement to be an off-axis aspherical reflective surface. It would perform a crucial role in minimizing the effect of Seidel Aberrations before the beam enters the camera (i.e., Hyperspectral Imager). Thus, it represented the smallest optical surface in the instrument. Hence, the component would demand only a brief amount of manufacturing time. Table 1 presents the optical parameters and specifications of TSC-1 M3 mirror.

Table 1. Specification of TSC-1’s Tertiary Mirror.

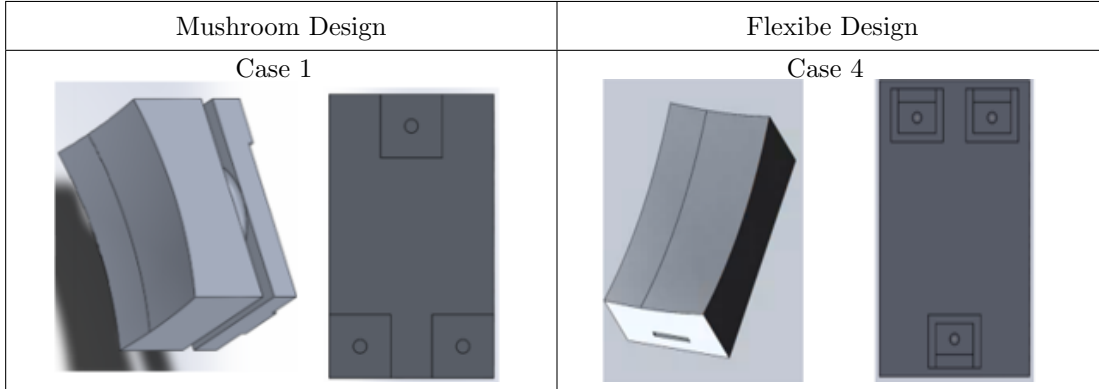
Parameter	Specification
Optical Surface dimension	$67.00 \pm 0.01 \text{ mm} \times 40.00 \pm 0.01 \text{ mm}$
Clear Aperture	$60.00 \pm 0.01 \text{ mm} \times 36.00 \pm 0.01 \text{ mm}$
Shape	Rectangle
Minimum Thickness	30.00 mm
Surface Type	Conical Surface, Concave
Radius of Curvature	$-120.156 \text{ mm} \pm 0.1\%$
Conic Constant	-0.188
De-center	6 mm
Surface Irregularity (PTV)	$< 500 \text{ nm}$
Mounting Features	$3 \times M3$ holes

2.2 Conventional Design

The objectives were to design and simulate the compact reflective surface for studying the relationship between mass and surface displacements as a result of screw pressure, polish pressure, and fundamental frequency. The prototypes were designed to be evaluated alongside the payload of TSC-1. However, the optical design of the TSC-1 payload has been updated as it evolved throughout the year, therefore the prototype design is no longer a like-for-like substitution of the M3 within the TSC-1 payload. Nevertheless, this design of freeform surface could be utilized in other payloads and future instruments. We compared the Mushroom and Flexible Pads designs both before and after mass reduction (without deforming the surface). The dimensions of the optical surface are $67 \text{ mm} \times 40 \text{ mm}$.

Within the Mushroom design, we created two mass-reduced subtypes: one with a series of circular punctures along its sides and another with a series of triangular punctures along its sides. On the other hand, we made a mass-reduced subtype from the Flexible Pads design by creating square punctures along the base of the prototype, namely the Conventional Flexible Pads design. By making small punctures, we ensure that the displacement of the optical surface would be minimal during the SPDT manufacturing process. Table 2 shows the blank models in Mushroom and Flexible designs before mass-reduction. We had not planned to polish the reflective surface during this project. However, the mirrors can be single-point diamond turned later. Since the modeling of the force applied to the optical surface during SPDT was complicated. We considered the polishing pressure, which is easier to estimate and should be a sufficient representative of the force that the mirror surface was subjected to.

Table 2. The starting point of the blank models in Mushroom and Flexible design before lightweight.



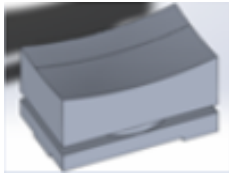
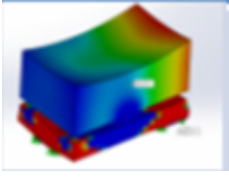
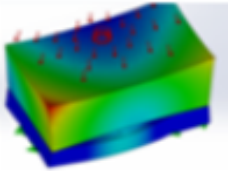
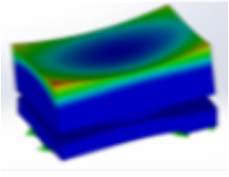
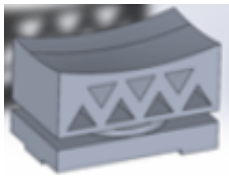
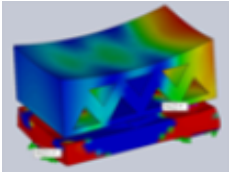
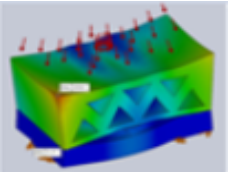
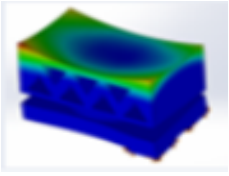
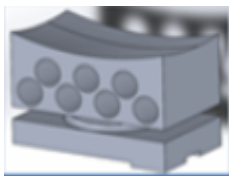
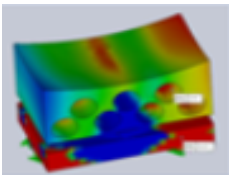
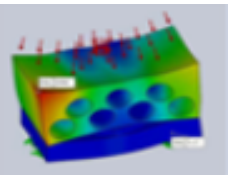
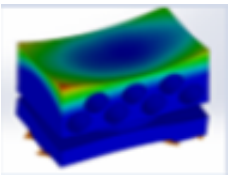

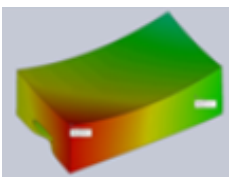
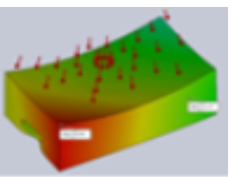
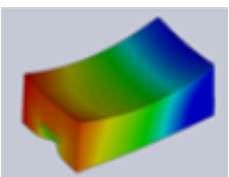
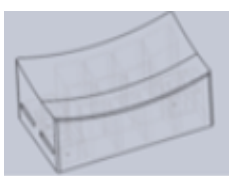
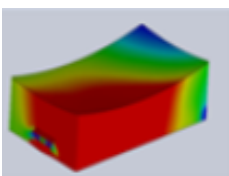
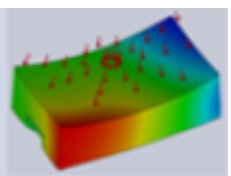
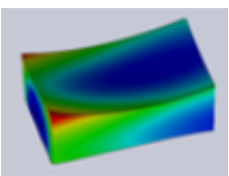
Column 1 and 2 represent the Mushroom design consisted of two connecting parts, which were the isolating optical surface and the mounting pads as shown on the left side of Table 2. The Flexible Pads design consisted of an isolated set of individual mounting surfaces and a flexible structure to absorb the local stress induced by the screws as shown on the right side of Table 2.

The main advantage of the Mushroom design was its sturdy solid structure, which was easy to machine and less likely to deform the optical surface. The drawback was its weight, especially as an optical component for space missions. On the other hand, the main advantage of the Flexible Pads design was the compactness of the mirror and its potential for further mass-reduction. But the main drawback was its lack of stiffness and low eigenfrequency, which suggested a higher risk for the amplification of surface deformation of the design during launch. For this reason, it was crucial to check the performance of the Flexible Pads design when subjected to vibrations and calculate the modal frequencies.

In this section, we summarized the parameters used with FEA, which would determine the level of deformation induced by the mounting screws and the polishing pressure. We also explained how to compute the first eigenfrequency in modal analysis and compared its value with the standards in the space industry.

Two types of stress-free designs were compared in this section. First, a solid but heavier design called “Mushroom” was studied. Due to the stiffness of the blank, this type of design displayed minimal deformation under stress induced by mounting screws or polishing tools. However, the blank is heavier than another option. Thus, it might not be an ideal flight design. A more compact design using Flexible Pads had also been analyzed and compared. This type of design had the advantage of being much lighter. But the pads could be an issue in the presence of strong vibration, such as during launch.

Table 3. A summary of the results obtained from the 5 case studies.

#	Design	Mass [g]	Screw Pressure [μm]	Polish Pressure [μm]	Fundamental Frequency [Hz]
1		264.3	 Max:0.27 Min:0.21	 Max:0.03 Min:0.01	 3767.5
2		220.5	 Max:0.26 Min:0.22	 Max:0.03 Min:0.02	 4078.5
3		195.8	 Max:0.15 Min:0.11	 Max:0.04 Min:0.01	 4301.5
4		135.0	 Max:0.35 Min:0.18	 Max:0.29 Min:0.12	 1863.6
5		72.6	 Max:0.39 Min:0.14	 Max:0.13 Min:0.08	 2152.0

Within Table 3, column 2 represents the CAD model in Mushroom and Flexible Pads designs divided into 5 models for the Conventional Manufacturing process; column 3 represents the total mass in grams of each model, after applied aluminum material properties. Columns 3, 4, and 5 show the total displacements from the FEA simulation results (i.e., screw force, polishing pressure, and fundamental frequency), where the color scales in the figures represent the displacement levels (red and blue for maximum and minimum displacements, respectively).

2.3 Additive Manufacturing Design

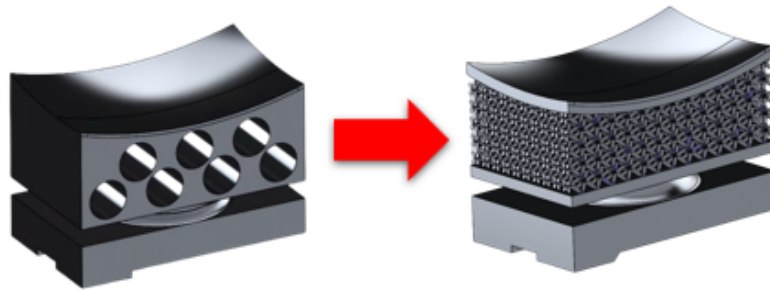


Figure 2. **Left:** the Mushroom design for the Conventional Manufacturing process. **Right:** the Mushroom design for the Additive Manufacturing process. Originally, the Mushroom design aimed for the Conventional Manufacturing process. However, we continue to reduce mass and strengthen the prototype by constructing lattices under the optical surface.

According to the Mushroom design's FEA results, the design was geared toward the Conventional manufacturing process. However, we continue to reduce mass of the model by applying the lattices inside the model as shown in Figure 2.

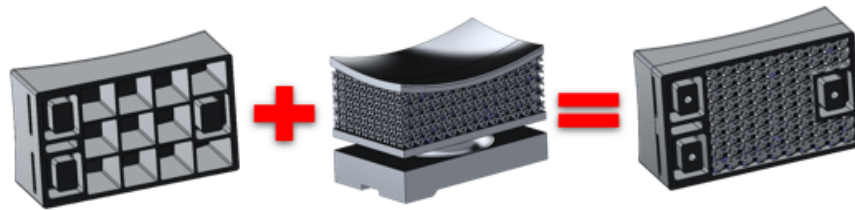
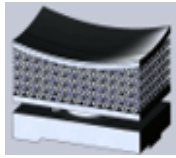
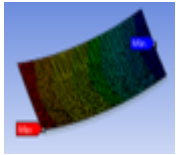
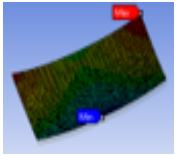
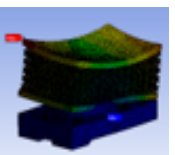
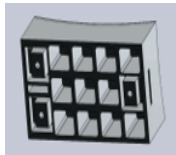
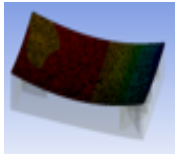
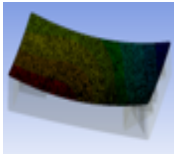
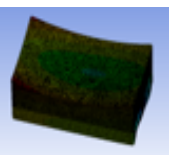
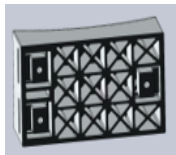
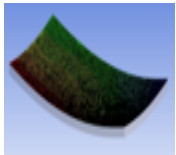
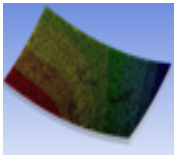
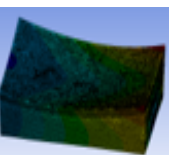

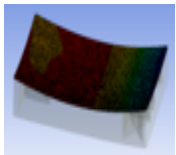
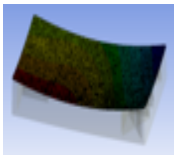
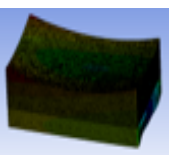


Figure 3. The lattices design was applied to the Flexible Pads design by maintaining the outer pads and adding the lattices in between, thus creating AM Flexible Pads (Lattices).

2.4 Designs Selection

Before we arrived with the AM Mushroom (Lattices) design from Model C: C1.00 mm, we had 19 case studies, which were derived from the three main models (i.e., Model A, Model B, and Model C). The different conditions of each model depended on the size, diameter of the lattice core, and number of lattices. The diameter of the lattices core of model A was between 0.50 mm to 2.25 mm, with total case studies of 9 cases. The diameter of the lattices core of model B was between 0.50 mm to 2.00 mm, with total case studies of 5 cases. The diameter of the lattices core of model C was between 0.50 mm to 2.00 mm, with total case studies of 5 cases. We calculated the FEA results using ANSYS software with 4 final designs selected.

Table 4. A summary of the FEA in ANSYS results obtained on the final selected designs.

Model	Design	Volume [cm^3]	Mass (Reduced) [g]	Screw Pressure [μm]	Polishing Pressure [μm]	Fundamental Frequency [Hz]
AM Mushroom Design (Lattice)		59.06	159.47 (59.73%)	 Max:0.46 Min:0.19	 Max:0.10 Min:0.05	 3658.8
Conv. Flexible Pads Design		26.88	72.57 (46.24%)	 Max:0.03 Min:0.02	 Max:0.43 Min:0.16	 2052.0
AM Flexible Pads Cross- Design		29.39	79.35 (41.22%)	 Max:0.07 Min:0.02	 Max:1.40 Min:1.07	 5416.9
AM Flexible Pads (Lattice)		26.20	70.73 (47.61%)	 Max:0.09 Min:0.07	 Max:0.42 Min:0.16	 2146.6

Within Table 4, column 1 illustrates the models built using Additive Manufacturing and Conventional Manufacturing process. Columns 2, 3, 4, and 5 show the CAD models in Solidworks, the total volumes of the models in cm^3 , the mass as the products of the aluminum density and the model volumes, and the mass reduction of the model. Column 6, 7, and 8 show the FEA simulation results on the screw force, polishing pressure, and fundamental frequency. The colors in the simulation figure present the displacement results. The red and blue contours indicate the maximum and minimum displacements, respectively. For example, the first model is AM Mushroom (Lattices) design that has a total mass of 159.47 g, with a mass reduction percentage of 59.73%, the displacement as a result of screw pressure and polishing pressure were less than 0.46 and 0.1 microns, respectively. While the frequency mode was 3658.8 Hz.

3. FINITE ELEMENT ANALYSIS

3.1 FEA Input Parameters

3.1.1 Screw Pressure

We had to limit the stress induced by the process of attaching screws to the mirror, which could propagate from the mounting plane to the optical surface. To quantifying this deformation (via FEA), the axial force applied to the screws must be calculated.

The axial force could be derived from torque. As a guideline, the torques applied on the screws should always be less than 70% of their maximum recommended values, which are 0.20, 0.40, 0.70, 1.60, 3.20, and 5.40 for M2, M2.5, M3, M4, M5, and M6 screws, respectively. To calculate the axial force applied by a specific torque, one can use Equation 1.

$$T = K \times F \times d \quad (1)$$

Where T represents wrench torque in the unit of [Nm], d is the fastener bolt's major diameter, and K is static friction coefficient. The values of K are 0.2, 0.16, and 0.16-0.17 for Steel, Cadmium, and Lubricated surfaces, respectively. For instance, in the case study where M3 screws were used, the maximum wrench torque was 0.70 N.m.

One can calculate the corresponding axial force of steel material using the example as illustrated in Equation 2.

$$F = \frac{T}{kd} = \frac{0.7 \text{ N m}^{-1}}{(0.2 \times 0.003 \text{ m})} = 1166 \text{ N} \quad (2)$$

The axial force generated by steel M3 screws should therefore be less than or equal 816.2 N or upto 70% of 1166 N.

3.1.2 Polishing Pressure

To estimate the deformation on the optical surface induced during the polishing, a pressure of 3.5 kPa was applied to the optical surface and an FEA was performed. This was a typical polishing pressure estimated in metallic mirror polishing.²⁵ The FEA results taken from one of the case studies is illustrated in Figure 4. The surface displacement and the pressure vector applied to the optical surface, with the fixed constraint surfaces can also be seen below.

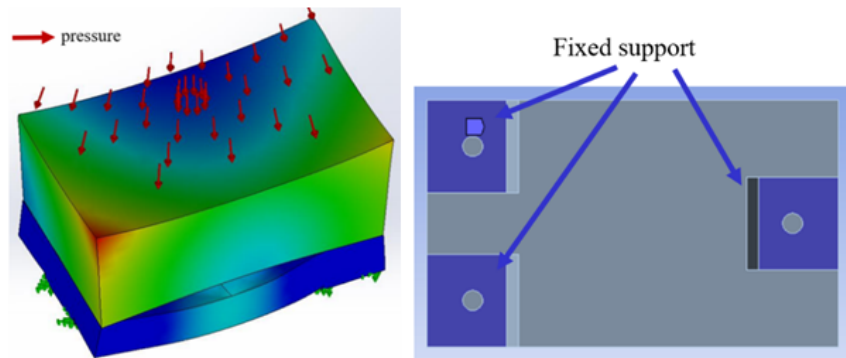


Figure 4. Left hand side: the pressure was applied with the model. Right hand side: the Fixed support was applied with the model.

3.2 FEA Data Processing

Once the FEA output files describing the optical surface displacement were produced, they were processed to decompose the displacement map into Zernike modes. The first stage was to remap the FEA mesh sampling into a rectangular grid of pixel size 0.5mm. Then, the data was fitted with a 7th order polynomial (36 terms). The residual print through created by the AM structure behind the optical surface was obtained by subtracting the surface displacement with the Zernike fit. Because of the high spatial order of the fit, only was left the even higher order displacement, related to the spatial frequency of the AM structure behind the surface or the pads.

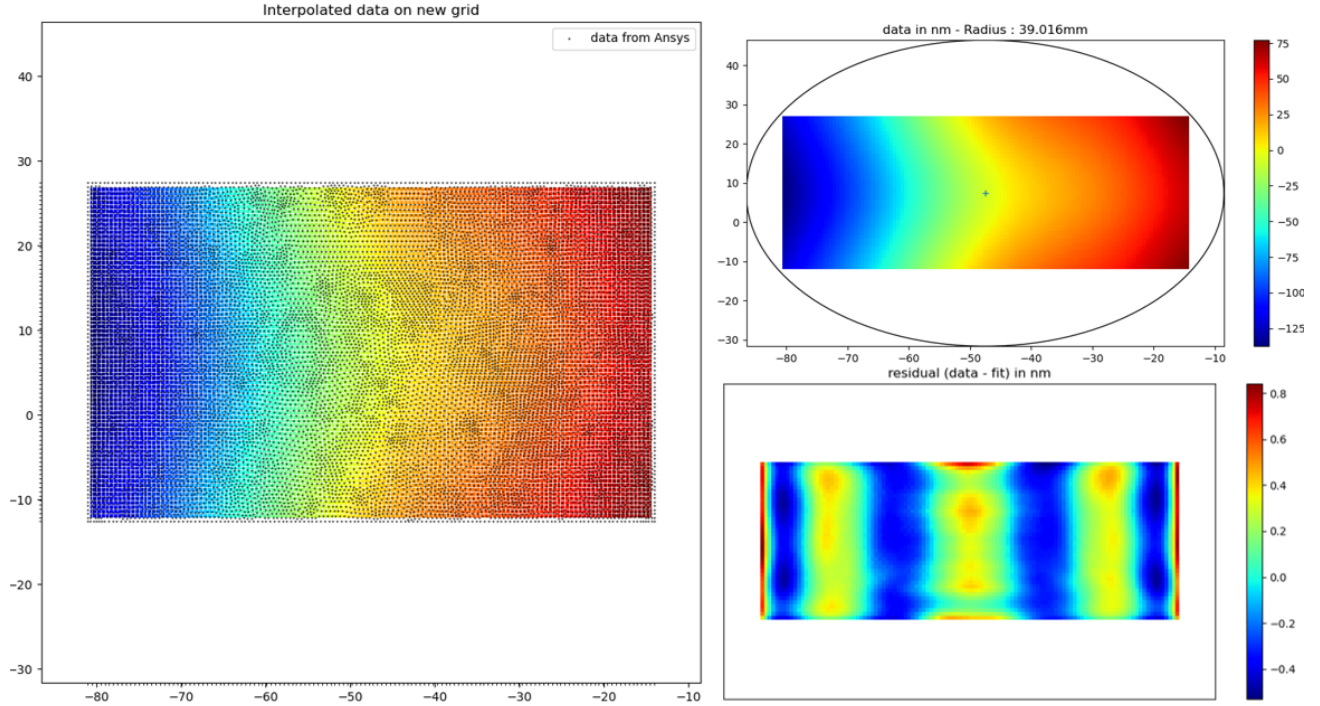


Figure 5. Left: Resampling for Design 1 from the non regular FEA mesh to a rectangular grid, Top Right: unit circle on which, the Least square fit is performed. Bottom Right : Print Through resulting from the subtraction of the FEA data with the Zernike fit of order 7

Figure 5 shows the various steps that were performed during the processing. Figure 5 *left* shows the remap of the FEA data computed from a non regular mesh to a rectangular grid of sampling 0.5mm. The black dots correspond to the nodes of the mesh and the white square are the pixel of the new rectangular grid. Figure 5 *top right* shows the unit circle on which the fit was performed, then Figure 5 *bottom right* shows the print through after subtraction of the 36 Zernike terms to the displacement map.

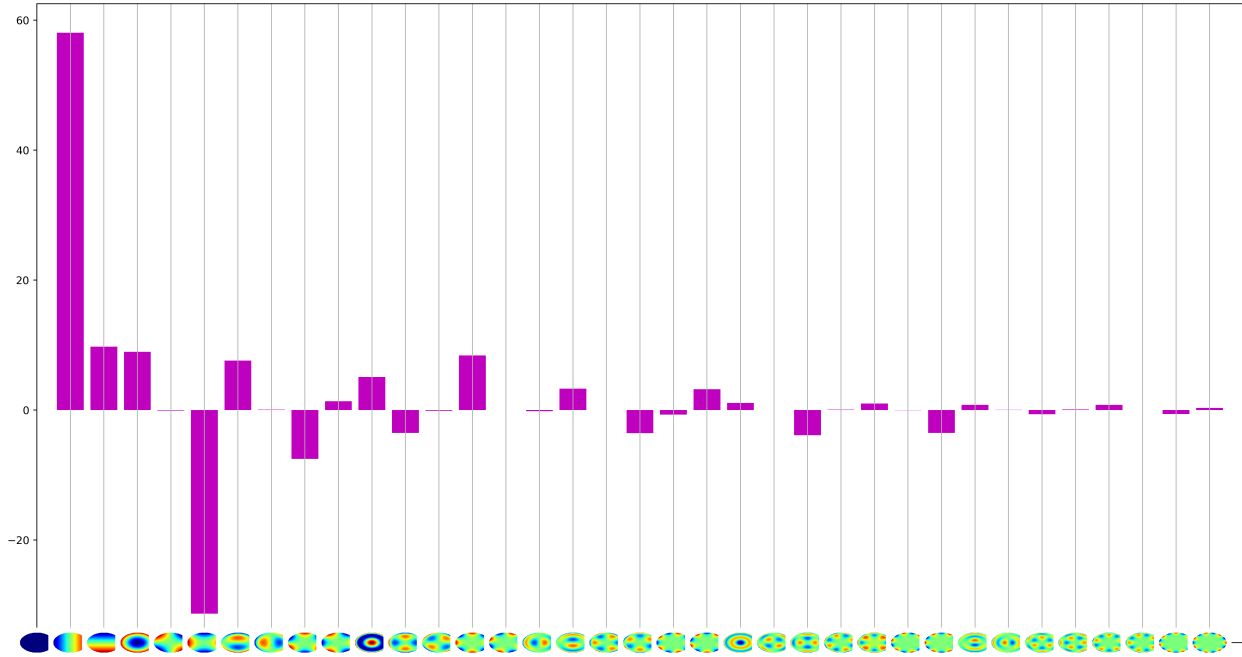


Figure 6. Display of the 36 Zernike Standard coefficients for Design 1 FEA data.

Figure 6 shows the decomposition of the displacement mp into 36 standard Zernike modes. The larger term, after Tip, Tilt and Defocus is Z6, the first order astigmatism at 0° .

3.3 FEA Results

The Zernike polynomials in Python were used to simulate the results represent in the displacement PV, RMS, Main Zernike Order and Print through of the optical surface. The print through of the model represent in Figure 7. The summary result in Table 5 present the displacement PV with Tip Tilt and Defocus, displacement without Tip Tilt and Defocus in micron unit, RMS value without Tip Tilt and Defocus and the main Zernike order. The print through of the Mushroom sub-design C 1.00 mm in screw pressure results present in Figure 7(a.). The print through of the Flexible Pads in screw pressure results present in Figure 7(b.). The print through of the Flexible Pads with cross design in screw pressure results present in Figure 7(c.). The print through of the Flexible Pads with lattices design in screw pressure results present in Figure 7(d.). The print through of the Mushroom sub-design C 1.00 mm in polishing pressure results present in Figure 8(a.). The print through of the Flexible Pads in polishing pressure results present in Figure 8(b.). The print through of the Flexible Pads with cross design in polishing pressure results present in Figure 8(c.). The print through of the Flexible Pads with lattices design in polishing pressure results present in Figure 8(d.). The Flexible Pads design provided the lowest displacement PV with and without Tip Tilt and Defocus and RMS without Tip Tilt and Defocus. All of the design in Table 5 have main Zernike Order in Z6(Astigmatism).

Table 5. A summary of the Zernike polynomial in screw pressure results obtained on the final 4 designs.

Design	Displacement PV incl. TTD [μm]	Displacement PV excl. TTD [μm]	RMS excl. TTD [μm]	Main Zernike Order
MushroomC- Mesh1.0mm-SP 	0.137	0.042	0.011	Z6 (Astigmatism)
Flexible Pads-SP 	0.009	0.003	0.001	Z6 (Astigmatism)
Flexible Pads- Cross-SP 	0.053	0.017	0.004	Z6 (Astigmatism)
Flexible Pads- Small-Lattices-SP 	0.024	0.014	0.004	Z6 (Astigmatism)

TTD is short for Tip/Tilt/Defocus

With reference to Table 6, the 1st column presents the name and CAD model of the case study designs of the 4 models that were selected. Columns 2nd and 3rd present the displacement PV including Tip, Tilt, defocus, and excluding Tip, Tilt, defocus calculated the result with Python code. 4th column presents the RMS value without Tip, Tilt, and defocus. Column 5th presents the heightened Zernike polynomial values, and the last

column presents the print through, the figure as shown in the figure below this table.

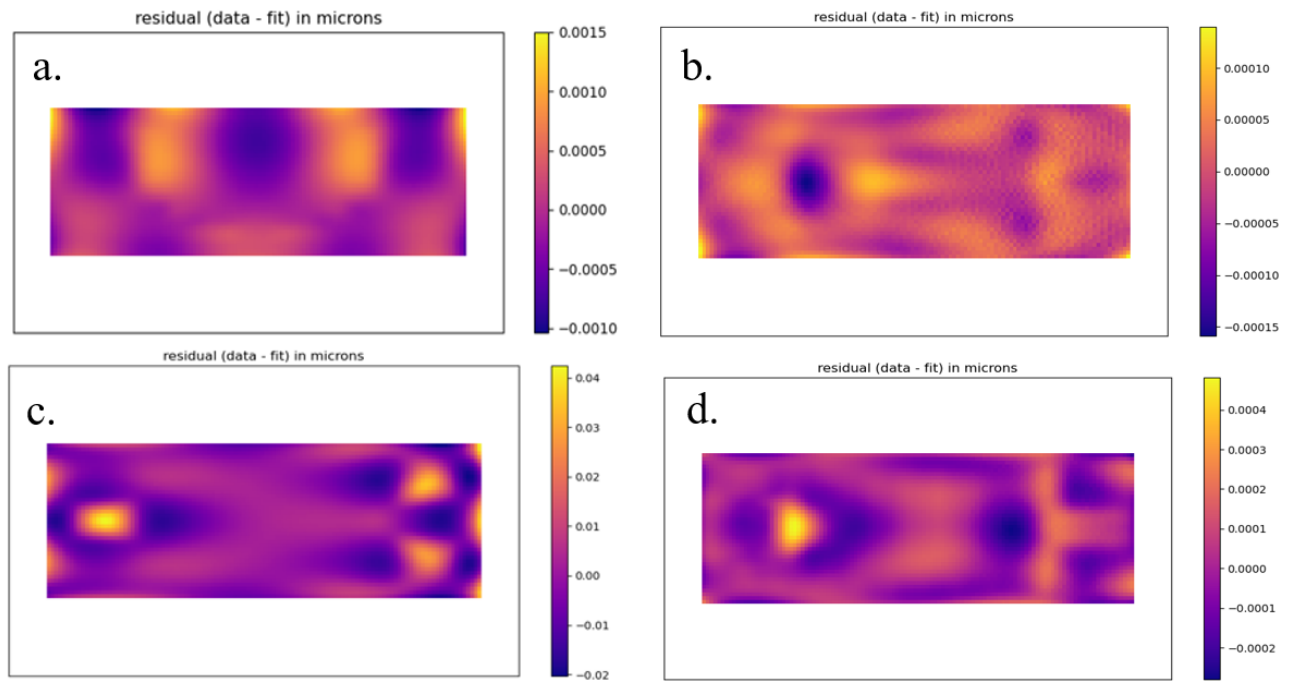


Figure 7. Present the print through of the mirror design separated into 4 models according to the Table 5.

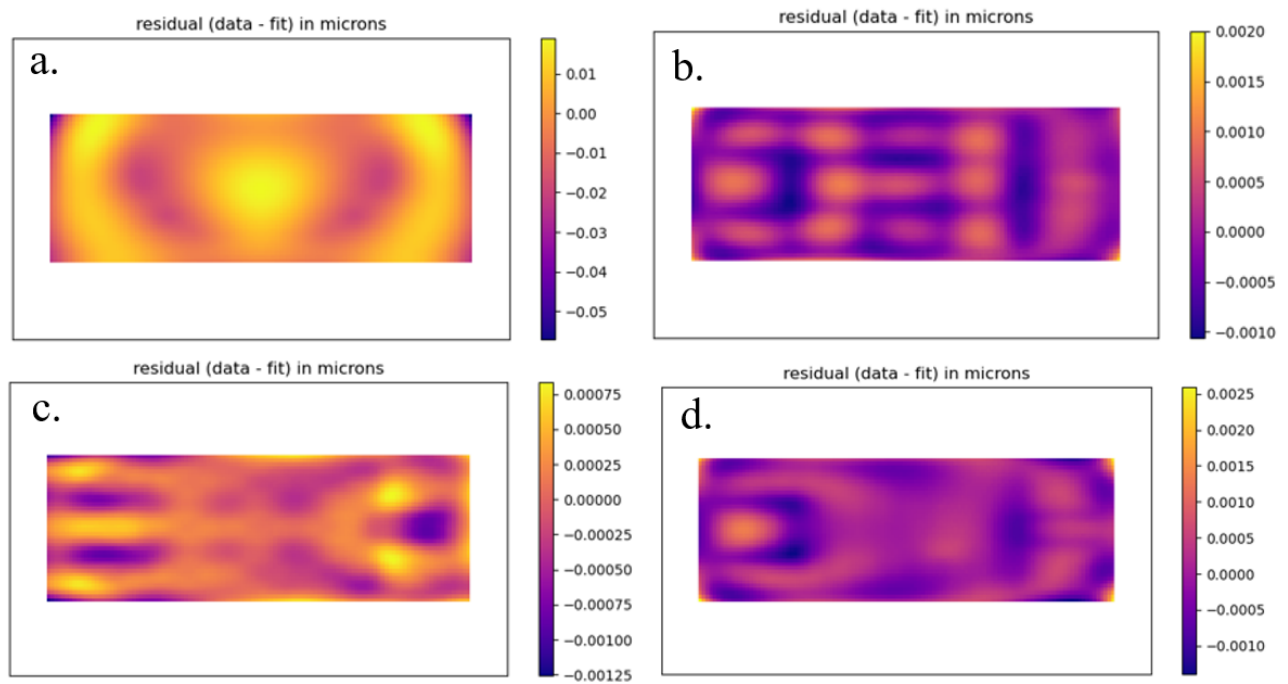


Figure 8. Present the print through of the mirror design separated into 4 models according to the Table 6.

Table 6. A summary of the Zernike polynomial in polishing pressure results obtained on the final designs.

Design	Displacement PV incl. TTD [μm]	Displacement PV excl. TTD [μm]	RMS excl. TTD [μm]	Main Zernike Order
MushroomC- Mesh1.0mm-PP 	0.792	0.501	0.097	Z6 (Astigmatism)
Flexible Pads-PP 	0.270	0.046	0.013	Z6 (Astigmatism)
Flexible Pads- Cross-PP 	0.255	0.055	0.015	Z6 (Astigmatism)
Flexible Pads- Small-Lattices-PP 	0.254	0.050	0.014	Z6 (Astigmatism)

TTD is short for Tip/Tilt/Defocus

4. ADDITIVE MANUFACTURE

4.1 The Print Process

Following the selection of the AM optimised designs, Mushroom, Flexible Pads - Cross, and Flexible Pads - Lattice, the designs were prepared for AM. The CAD for each design was converted into an STL file, loaded within the Aconity printer software, located digitally upon the build plate and support material digitally added where necessary. Following a digital set-up of the parts, the printer parameters are set and the printer prepared for build - such as ensuring adequate powder is within the hopper. When the build starts the first few layers are critical and they are therefore observed until there is confidence that all the set parameters have converged to an optimum build strategy. Table 7 outlines the specification of the Aconity printer used in this study.

Figure 9 (*top and bottom right*) highlights the challenges in achieving a successful build. Aluminium is a difficult metal to print in due to its high thermal conductivity and therefore several failed builds were encountered. However, after a period of iteration, the project successfully printed a series of prototypes, as demonstrated in Figure 9 *bottom right*. The next step in the AM process chain is subtractive machining (mill, drill & lathe) of the critical surfaces of the AM substrates to prepare them for SPDT, as shown in Figure 10.

Table 7. Specification of the Aconity metal 3D printer.

Parameter	Specification
Build Space	$\phi 170\text{ mm} \times H200\text{ mm}$
Laser Configuration	Up to 2× Single Mode 400 W / 500 W / 700 W / 1000 W
Optics configuration/Spot size	3D Scanning/80-500 μm
Process monitoring options	Coaxial Pyrometer Coaxial High-Speed CMOS
Layer Thickness	Down to 10 μm
Max Scan Speed	12 m/s
Gas Type / Pressure	Argon / 4.6-6 Bar
Residual Oxygen Content	< 100ppm
Pressurized Air Type/Pressure	ISO 8573-1:2010 [1:4:1] / 6 Bar
Pressurized Air Consumption	< 5L/min

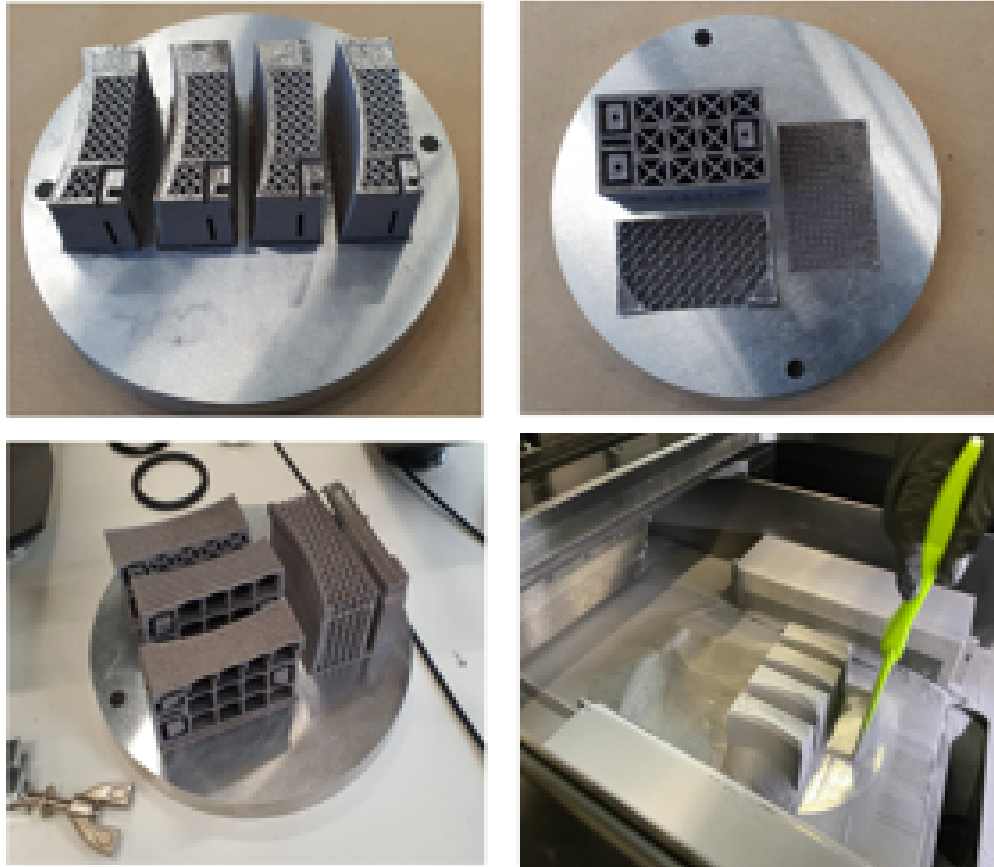


Figure 9. A trial and error process before getting the perfect piece.

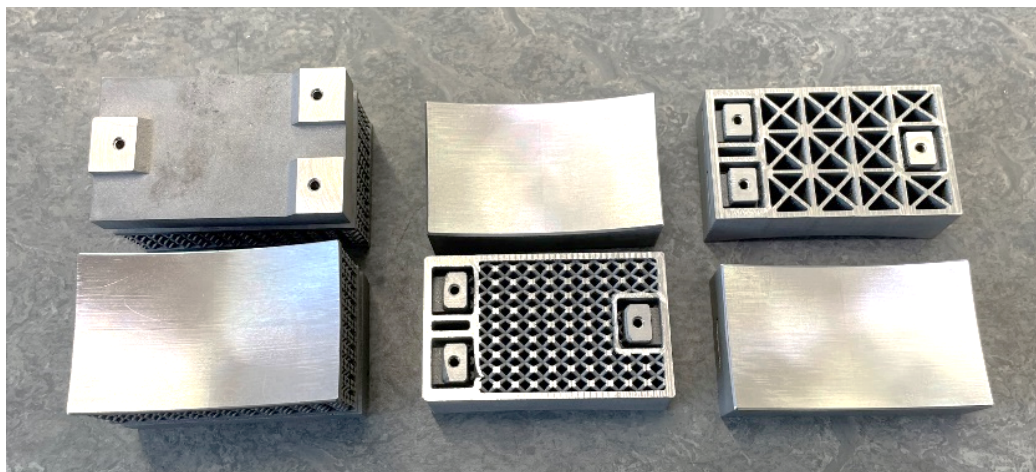


Figure 10. Model after post-machining optical surface.

5. DIAMOND MACHINING

This section reports on the diamond machining activities, the form optimization for both rotationally and non-rotationally symmetric errors and the machining parameters optimization. The sequence of the actions is reported on Figure 11.



Figure 11. Diamond machining activities of TSC-1's M3 mirror.

Starting with the tool alignment, the diamond tip was referenced to the spindle axis on both x and y directions using the feedback from form measurement of a spherical test stud. Once aligned, the mirror attached onto its backing plate was then placed on the spindle and balanced. A tool path program was prepared, using a point cloud definition to allow for freeform correction later during the finishing process. At this stage, to facilitate metrology, the freeform shape defined by the parameters given in Table 1, was approximated by the best fit sphere to a diameter of 72mm: Radius of curvature at 120.67mm. That way, the mirror form was checked against a F/1.5 reference spherical beam on a Zygo Verifire.

A rough cut, a semi-finish and a finish cut were applied, and the mirror form deviation was measured. A new program was then produced, which considered the residual form error and this process was repeated until the

form figure was less than 45nm RMS. The form optimization used low order Zernike polynomial decomposition, to only keep the low frequency on the correction. Roughness was measured with a Zygo Zegage Plus equipped with x20 objective. Finally, the blanks were cleaned with CO₂ and Acetone before they were released from their machining fixtures. At this stage, we performed another form measurement with screws released, and with screws retorqued to the nominal values to investigate if the mirror’s form error induced by the mounting screws could be reversed by applying the nominal torque as the once applied during machining. A summary of these 3 form errors for the 4 designs is given in the next section.

6. METROLOGY AND DISCUSSIONS

6.1 Form Error Analysis

The high order form distortion (for Zernike order larger than 7) has been discussed in Section 3.3 and is displayed on Figure 7 *a, b, c* and *d*, for stress induced by the mounting screws, and on Figure 8 *a, b, c* and *d*, for stress induced by polishing or machining stress for the 4 designs. In this section we look at the residual low order form distortion when the mirrors are detached from their machining fixture.

Since the mirror surfaces were machined to a best fit sphere profile and measured at the centre of curvature, Tip/Tilt/Power were removed from the interferometer measurement to account for residual decenter and focus misalignment.

In the following, we compare the computed residual distortion induced by the stress caused by the screws (for a torque of 0.5Nm) with tip, tilt, and defocus removed with the measured distortion. The latter was computed by subtraction of the measurements when the mirror was free mounted and when it was attached. Finally, we retorqued the mirror to the original torque, and compared the distortion with the initial measurement.

6.1.1 Design 1: Mushroom Type

For the Design 1 (Mushroom type), the main distortion is astigmatism.

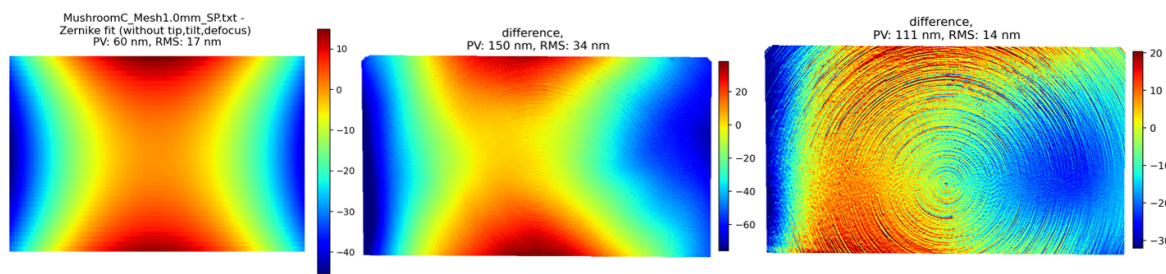


Figure 12. Design 1 comparison between FEA modelling and measurements with piston, tip, tilt and defocus removed. Colorbar in nm, clipped at 2σ . Left – Surface displacement modelled by FEA. Middle - Difference between the measurements with the 3 interface screws released and with the 3 interface screws torqued at 0.5Nm. Right - Difference between the measurements with the 3 interface screws retorqued (after being totally released) and with the screws initially attached.

With 3 screws torqued at 0.5 Nm, the FEA produces an astigmatic distortion of about 60 nm PV and 17 nm RMS (Figure 12 *left*). This type of deformation agrees well with the measurement (Figure 12 *middle*), although the amplitude is different, being more than twice the theoretical value. The reason could be that the force load applied to the tapped holes to model the stress during the FEA was a limited representation of the effect that occurs in reality. Once retorqued (Figure 12 *right*), the mirror surface went back into its original shape, to within 15 nm RMS (most of the amplitude in this figure resulting from the lines being amplified by the subtraction operation – the two images could have been slightly shifted).

6.1.2 Design 2: Conventional Design

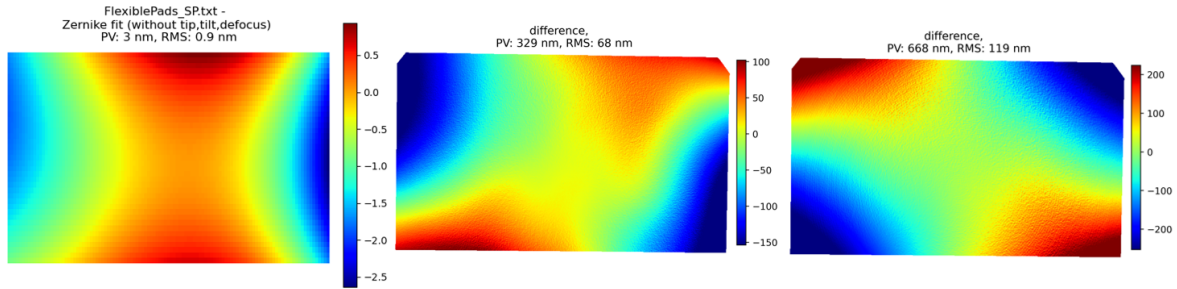


Figure 13. Design 2 comparison between FEA modelling and measurements with piston, tip, tilt and defocus removed. Colorbar in nm, clipped at 2σ . Left – Surface displacement modelled by FEA. Middle – Difference between the measurements with the 3 interface screws released and with the 3 interface screws torqued at 0.5Nm. Right – Difference between the measurements with the 3 interface screws retorqued (after being totally released) and with the screws initially attached.

For the conventional design, the FEA modelled distortion remains quite low (around 3 nm PV) demonstrating that, in principle, the flexible pads are doing their job of isolating the stress from propagating to the optical surface - Figure 13 *left*. However, once the blank is detached, Figure 13 *middle* shows that a distortion of around 330 nm PV and 68 nm RMS was measured. Similarly, when the 3 screws are retorqued to their nominal value, the deformation was not corrected but amplified. One hypothesis was that each of the 3 pads had a residual tilt created during CNC machining or by the tapped hole direction not being normal to the pad plane. This problem was not removed during the flycutting process. As a result, the blank was machined under stress at the 3 tapped holes level. When the screws were removed, the stress was then released and propagated to the optical surface. This could also explain the fact that when retorqued, the distortion was not corrected but amplified.

6.1.3 Design 3: Flexible Pads – Cross Design

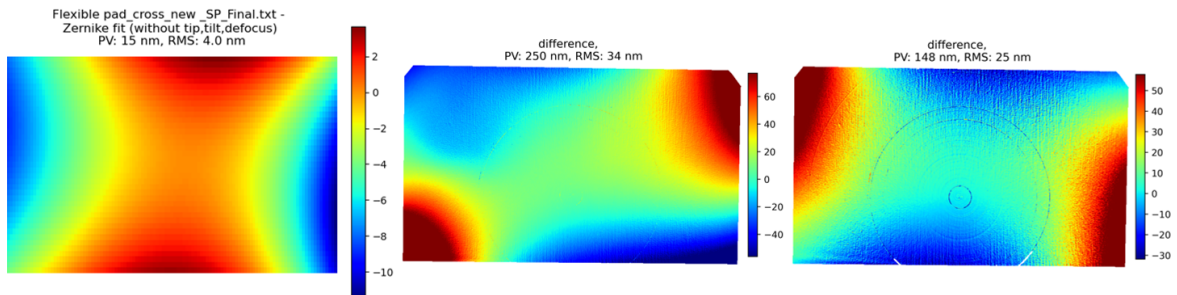


Figure 14. Design 3 comparison between FEA modelling and measurements with piston, tip, tilt and defocus removed. Colorbar in nm, clipped at 2σ . Left – Surface displacement modelled by FEA. Middle – Difference between the measurements with the 3 interface screws released and with the 3 interface screws torqued at 0.5Nm. Right – Difference between the measurements with the 3 interface screws retorqued (after being totally released) and with the screws initially attached.

The cross design (design 3) is similar to the design 2, in the sense that the measurement (Figure 14 *middle*) shows a much stronger distortion than the one given by the FEA modelling (Figure 14 *left*). It also shows the astigmatic deformation in the opposite direction than expected. However, when the screws are retorqued, a fraction of the deformation is corrected.

6.1.4 Design 4: Flexible Pads – Lattice Design

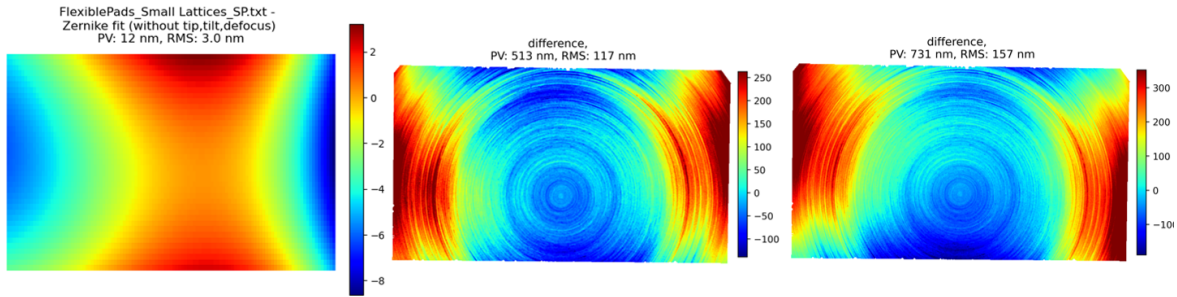


Figure 15. Design 4 comparison between FEA modelling and measurements with piston, tip, tilt and defocus removed. Colorbar in nm, clipped at 2σ . Left – Surface displacement modelled by FEA. Middle – Difference between the measurements with the 3 interface screws released and with the 3 interface screws torqued at 0.5Nm. Right – Difference between the measurements with the 3 interface screws retorqued (after being totally released) and with the screws initially attached.

The design 4, with the lattice design, is similar to Designs 2 and 3. This design also displays a stronger measured distortion than the one expected with the FEA modelling (Figure 15 left). These 3 designs seems to point out an issue with the tapped holes or the pads plane which sends a stress into the blank as shown on the measurement of the optical surface (Figure 15 middle and right).

6.2 Roughness and Cosmetic

The Design 2, which is the only non-AM part among our 4 case studies, was made in RSA 6061 and served as a reference in term of surface finish when compared to the AM alloy and their behaviour during single point diamond turning. A typical roughness measurement, after applying a High pass filter of cutoff frequency of 10 mm^{-1} is given on Figure 16.

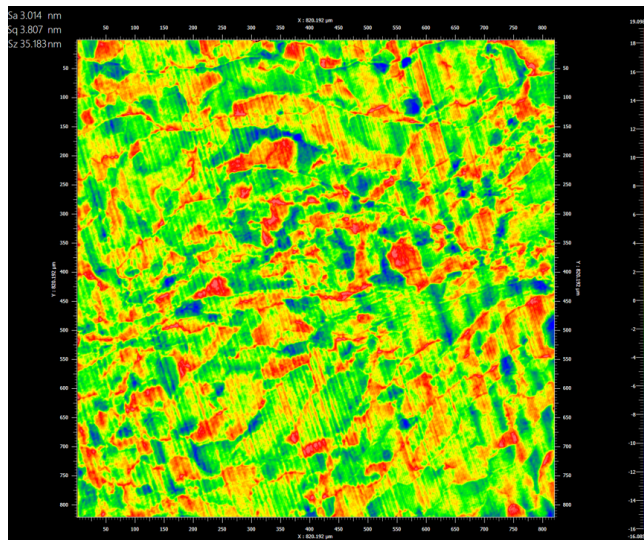


Figure 16. Roughness measured after a finish pass, on the Design 2. The roughness is typically 4 nm RMS.

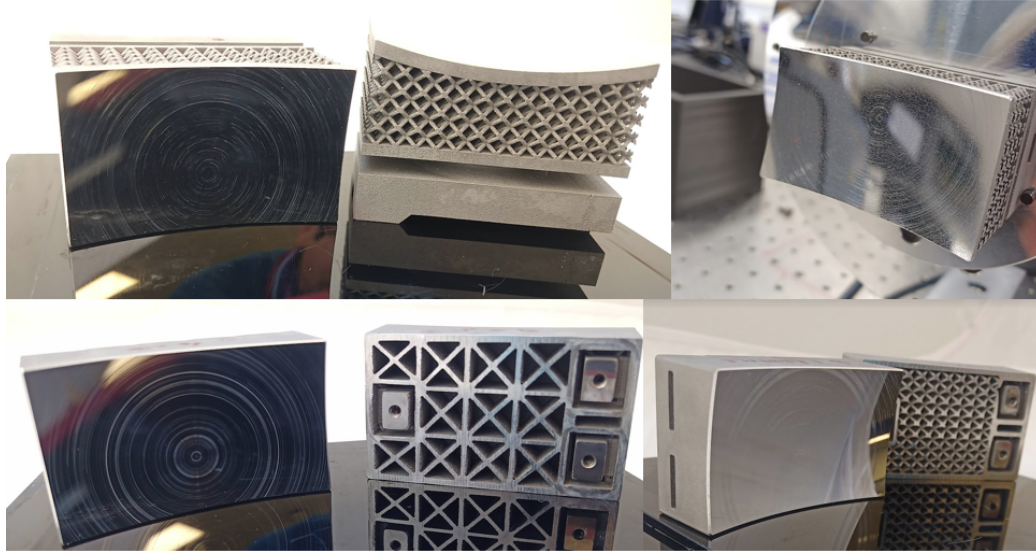


Figure 17. cosmetic issues on the 3 AM design parts. Top Left is one Mushroom type design with pick up marks (harder particles of material being dragged on the surface). – Top Right is another Mushroom type mirror with a significant number of pores on the surface. – Bottom Left: Design 3 with cutting marks - Bottom Right : Design 4 with cutting marks.

The 3 AM prototypes did not exhibit a good finish with a mix of machining marks and/or pores visible on the surface, as shown in the Figure 17. It is likely that the machining marks (comet tails) are due to a ‘lack of fusion’ within the part and the diamond tool picking up loose material and dragging it along the surface. The porosity is a common defect within AM and it can be present due to a lack of fusion or by too much heat, in this case, given the machining marks, a lack of fusion is suspected. To improve the surface in the future, alternative printer settings can be utilised to minimise the lack of fusion, furthermore, heat treatments, such as hot isostatic pressing (HIP) can be used to close porosity within the AM parts.²⁹

7. CONCLUSION

The ultimate goal of this project was knowledge exchange between the UK and Thailand in the design and manufacture of metal freeform mirrors for astronomy and Earth observation. The objective of the project was to achieve the project goal via the means of a joint Thailand-UK case study - namely the lightweight redesign and manufacture of prototypes replicating the M3 mirror within the TSC-1 satellite. The project has been successful in this objective, four prototype mirrors (1 CM design and 3 AM designs) were delivered within this project and importantly, the project was implemented by the NARIT engineers with support from the UK institutes.

The delivered prototypes provide a further dataset in the development of AM mirrors and in their comparison to conventional mirrors. However, there is still further investigation required to understand the discrepancy with the FEA results in comparison to the SPDT results and how to improve the surface roughness of the AM mirrors.

ACKNOWLEDGMENTS

The team acknowledges the 2019 STFC – NARIT Newton Fund, grant numbers ST/T007133/1, ST/T006005/1 and ST/T006552/1, for enabling the research, collaboration and knowledge exchange. The authors also acknowledge the EPSRC Future Manufacturing Hub in Manufacture using Advanced Powder Processes (MAPP) grant number EP/P006566/1. C. Atkins acknowledges the UKRI Future Leaders Fellowship program, grant MR/T042230/1, for continued participation in this project. R Snell acknowledges the EPSRC Future Manufacturing Hub in Manufacture using Advanced Powder Processes (MAPP) EP/P006566/1 and the Henry Royce Institute for Advanced Materials, funded through EPSRC grants EP/R00661X/1, EP/S019367/1, EP/P02470X/1 and EP/P025285/1.

REFERENCES

- [1] Thompson, K. P. and Rolland, J. P., “Freeform Optical Surfaces: A Revolution in Imaging Optical Design,” *Optics and Photonics News* **23**(6), 30 (2012).
- [2] Bourgenot, C., Robertson, D. J., Stelter, D., and Eikenberry, S., “Towards freeform curved blazed gratings using diamond machining,” **9912**, 99123M (2016).
- [3] Challita, Z., Agócs, T., Hugot, E., Jaskó, A., Kroes, G., Taylor, W., Miller, C., Schnetler, H., Venema, L., Mosoni, L., Mignant, D. L., Ferrari, M., and Cuby, J.-G., “Design and development of a freeform active mirror for an astronomy application,” *Optical Engineering* **53**(3), 1 – 11 (2014).
- [4] Hugot, E., Wang, X., Valls-Gabaud, D., Lemaître, G., Agócs, T., Shu, R., and Wang, J., “A freeform-based, fast, wide-field, and distortion-free camera for ultralow surface brightness surveys,” in [*Space Telescopes and Instrumentation 2014: Optical, Infrared, and Millimeter Wave*], Jr., J. M. O., Clampin, M., Fazio, G. G., and MacEwen, H. A., eds., **9143**, 1513 – 1523, International Society for Optics and Photonics, SPIE (2014).
- [5] Zhang, X., ping Zhang, J., wei Shi, G., xiong Wu, Y., jie Wang, L., Zeng, F., meng Qu, H., zhen Zhang, J., bo Wu, H., Zhu, Y., and Wang, C., “Optical design of off-axis astronomical space telescope based on freeform surfaces,” in [*International Optical Design Conference 2014*], Figueiro, M., Lerner, S., Muschaweck, J., and Rogers, J., eds., **9293**, 198 – 205, International Society for Optics and Photonics, SPIE (2014).
- [6] Ries, H. and Muschaweck, J., “Tailored freeform optical surfaces,” *J. Opt. Soc. Am. A* **19**, 590–595 (Mar 2002).
- [7] Chrisp, M. P., Primeau, B., and Echter, M. A., “Imaging freeform optical systems designed with NURBS surfaces,” *Optical Engineering* **55**(7), 1 – 7 (2016).
- [8] Lemaître, G., Vola, P., and Muslimov, E., “Active optics in astronomy - freeform mirror for the messier telescope proposal,” (2019).
- [9] Muslimov, E., Bouret, J.-C., Neiner, C., Ariste, A. L., Ferrari, M., Vivès, S., Hugot, E., Grange, R., Lombardo, S., Lopes, L., Costeraste, J., and Brachet, F., “POLLUX: a UV spectropolarimeter for the LUVOIR space telescope project,” in [*Space Telescopes and Instrumentation 2018: Ultraviolet to Gamma Ray*], den Herder, J.-W. A., Nikzad, S., and Nakazawa, K., eds., **10699**, 33 – 45, International Society for Optics and Photonics, SPIE (2018).
- [10] Sironi, G., Canestrari, R., Giro, E., La Palombara, N., and Pareschi, G., “The cherenkov optics qualification facilities at inaf-oab laboratories,” *Nuclear Instruments and Methods in Physics Research Section A: Accelerators, Spectrometers, Detectors and Associated Equipment* **952**, 162163 (2020). 10th International Workshop on Ring Imaging Cherenkov Detectors (RICH 2018).
- [11] jun Zhang, X., xiang Hu, H., lin Xue, D., and Li, M., “Testing and alignment of freeform-based multi-mirror telescopes,” in [*Current Developments in Lens Design and Optical Engineering XVI*], Johnson, R. B., Mahajan, V. N., and Thibault, S., eds., **9578**, 75 – 83, International Society for Optics and Photonics, SPIE (2015).
- [12] Allington-Smith, J. R., Content, R., Dubbeldam, C. M., Robertson, D. J., and Preuss, W., “New techniques for integral field spectroscopy – I. Design, construction and testing of the GNIRS IFU,” *Monthly Notices of the Royal Astronomical Society* **371**, 380–394 (08 2006).
- [13] Purl, D. J., Lobb, D. R., Barnes, A. R., Talbot, R. G., Rolt, S., Robertson, D. J., Closs, M. F., and te Plate, M., “Flight model performance of the integral field unit for the James Webb Space Telescope’s near-infrared spectrograph,” in [*Modern Technologies in Space- and Ground-based Telescopes and Instrumentation*], Atad-Ettedgui, E. and Lemke, D., eds., **7739**, 410 – 420, International Society for Optics and Photonics, SPIE (2010).
- [14] Thompson, K. P., Schiesser, E., and Rolland, J. P., “Why are freeform telescopes less alignment sensitive than a traditional unobscured TMA?,” in [*Optifab 2015*], Bentley, J. L. and Stoebenau, S., eds., **9633**, 320 – 324, International Society for Optics and Photonics, SPIE (2015).
- [15] Rolt, S., Dubbeldam, C. M., Robertson, D. J., and Ryder, D. A., “Design for test and manufacture of complex multi-component optical instruments,” in [*Optical Fabrication, Testing, and Metrology III*], Duparré, A. and Geyl, R., eds., **7102**, 142 – 152, International Society for Optics and Photonics, SPIE (2008).

- [16] Atkins, C., van de Vorst, L. T. G. B., Farkas, S., Hugot, E., Mező, G., Morris, K., Roulet, M., Snell, R., Sanginés, F. T., Todd, I., Vega-Moreno, A., and Schnetler, H., “The OPTICON A2IM Cookbook: an introduction to additive manufacture for astronomy,” **12188-29**, International Society for Optics and Photonics, SPIE (2022).
- [17] Zhang, K., Qu, H., Guan, H., Zhang, J., Zhang, X., Xie, X., Yan, L., and Wang, C., “Design and fabrication technology of metal mirrors based on additive manufacturing: A review,” *Applied Sciences* **11**(22) (2021).
- [18] Sweeney, M., Acreman, M., Vettese, T., Myatt, R., and Thompson, M., “Application and testing of additive manufacturing for mirrors and precision structures,” *Proc. SPIE* **9574**, 957406–957406–13 (2015).
- [19] Herzog, H., Segal, J., Smith, J., Bates, R., Calis, J., De La Torre, A., Kim, D. W., Mici, J., Mireles, J., Stubbs, D. M., and Wicker, R., “Optical fabrication of lightweighted 3d printed mirrors,” *Proc. SPIE* **9573**, 957308–957308–15 (2015).
- [20] Atkins, C., Feldman, C., Brooks, D., Watson, S., Cochrane, W., Roulet, M., Doel, P., Willingale, R., and Hugot, E., “Additive manufactured x-ray optics for astronomy,” *Proc. SPIE* **10399**, 10399 – 10399 – 15 (2017).
- [21] Tan, S., Li, Q., Xu, Y., Shen, H., Cheng, Y., Jia, P., and Xu, Y., “Design and fabrication of lightweight additively manufactured mirrors for aviation,” *Appl. Opt.* **61**, 2198–2206 (Mar 2022).
- [22] Yan, L., Zhang, X., Fu, Q., Wang, L., Shi, G., Tan, S., Zhang, K., and Liu, M., “Assembly-level topology optimization and additive manufacturing of aluminum alloy primary mirrors,” *Opt. Express* **30**, 6258–6273 (Feb 2022).
- [23] von Lukowicz, H., Hartung, J., Hilpert, E., Damm, C., Peschel, T., and Heidler, N., “Optimization and additive manufacturing of a three-mirror-anastigmatic telescope,” in [*International Conference on Space Optics — ICSSO 2020*], Cugny, B., Sodnik, Z., and Karafolas, N., eds., **11852**, 67 – 78, International Society for Optics and Photonics, SPIE (2021).
- [24] Hilpert, E., Hartung, J., von Lukowicz, H., Herffurth, T., and Heidler, N., “Design, additive manufacturing, processing, and characterization of metal mirror made of aluminum silicon alloy for space applications,” *Optical Engineering* **58**(9), 1 – 9 (2019).
- [25] Atkins, C., Brzozowski, W., Dobson, N., Milanova, M., Todd, S., Pearson, D., Bourgenot, C., Brooks, D., Snell, R., Sun, W., Cooper, P., Alcock, S. G., and Nistea, I.-T., “Additively manufactured mirrors for CubeSats,” in [*Astronomical Optics: Design, Manufacture, and Test of Space and Ground Systems II*], Hull, T. B., Kim, D. W., and Hallibert, P., eds., **11116**, 335 – 352, International Society for Optics and Photonics, SPIE (2019).
- [26] Atkins, C., Feldman, C., Brooks, D., Watson, S., Cochrane, W., Roulet, M., Hugot, E., Beardsley, B., Harris, M., Spindloe, C., Alcock, S. G., Nistea, I.-T., Morawe, C., and Perrin, F., “Topological design of lightweight additively manufactured mirrors for space,” *Proc. of SPIE* **10706** (2018).
- [27] Tan, S., Ding, Y., Xu, Y., and Shi, L., “Design and fabrication of additively manufactured aluminum mirrors,” *Optical Engineering* **59**(1), 1 – 17 (2020).
- [28] Woodard, K. S. and Myrick, B. H., “Progress on high-performance rapid prototype aluminum mirrors,” in [*Advanced Optics for Defense Applications: UV through LWIR II*], Vizgaitis, J. N., Andresen, B. F., Marasco, P. L., Sanghera, J. S., and Snyder, M. P., eds., **10181**, 177 – 182, International Society for Optics and Photonics, SPIE (2017).
- [29] Snell, R. M., Atkins, C., Schnetler, H., Saunders, H., Beardsley, M., Harris, M., and Todd, I., “Towards understanding and eliminating defects in additively manufactured CubeSat mirrors,” **12188-28**, International Society for Optics and Photonics, SPIE (2022).